

Complete crystal field calculation of Zeeman-hyperfine splittings in europium

Kieran M. Smith,¹ Michael F. Reid,^{2,3} Matthew J. Sellars,¹ and Rose L. Ahlefeldt¹

¹*Centre for Quantum Computation and Communication Technology,*

Research School of Physics, The Australian National University, Canberra, Australia

²*School of Physical and Chemical Sciences, University of Canterbury, PB 4800, Christchurch 8041, New Zealand*

³*Dodd-Walls Centre for Photonic and Quantum Technologies, New Zealand*

(Dated: May 13, 2022)

Computational crystal field models have successfully predicted Zeeman hyperfine structure in several rare earth ions, but have not yet been applied to the Zeeman-hyperfine structure of Eu^{3+} . Modeling the structure of the $J = 0$ singlet levels in Eu^{3+} , in particular, requires the inclusion of the commonly omitted lattice electric quadrupole interaction and the nuclear Zeeman interaction. Here, we include these terms in a computational model to fit the crystal field levels and the Zeeman hyperfine structure of the 7F_0 and 5D_0 states in three Eu^{3+} sites: the C_{4v} and C_{3v} sites in CaF_2 and the C_2 site in $\text{EuCl}_3 \cdot 6\text{H}_2\text{O}$. Close fits are obtained, even in the low symmetry case. We also present a reduced spin Hamiltonian based on the crystal field model, without the normal assumption of no J mixing, and compare simulated and experimental spin Hamiltonians for the three sites.

I. INTRODUCTION

Crystals containing rare earth ions are now extensively studied for quantum information applications, particularly quantum memories. These applications almost always require precise knowledge of the hyperfine structure of the rare earth ion in the optical ground and excited states employed. In memory protocols such as the gradient echo memory [1] or the atomic frequency comb protocol [2], hyperfine structure information is used to spectrally prepare the memory by pumping population at specific frequencies into non-resonant hyperfine states. Knowledge of the hyperfine structure is also used to predict the locations of ZEFOZ (zero first order Zeeman) [3] points where hyperfine transitions are protected from dephasing caused by magnetic fluctuations, and to identify fields at which Λ transitions with favorable oscillator strengths for quantum memories can be obtained [4, 5].

Hyperfine structure is typically determined from experimental data recorded over a range of magnetic fields, which is then fitted to a reduced spin Hamiltonian that parameterizes any electronic contributions to the nuclear structure. This approach has been used very successfully, for instance, for predicting ZEFOZ points in $\text{Eu}^{3+}:\text{Y}_2\text{SiO}_5$ to extend the coherence time by six orders of magnitude [6]. However, there are both limitations and drawbacks to using reduced spin Hamiltonians. They cannot be applied when the electronic contributions to the nuclear structure are not constant, for instance for Kramers rare earth ions in over a large range of magnetic fields. The experimental data can also contain many lines, particularly for ions with high nuclear spin or in crystals with multiple magnetic subsites, which can be difficult to fit to a spin Hamiltonian, especially in the case of low symmetry where there are many free parameters. Finally, the spin Hamiltonian often provides little physical insight into the ion or the site.

An alternative is to use a full crystal field model for the whole $4f$ configuration of the rare earth ion, including interactions that generate hyperfine structure. These

types of models have been successfully applied for several different hosts doped with Kramers and non-Kramers rare earth ions, including Pr^{3+} [5, 7–10], Er^{3+} [11–14], Ho^{3+} [7, 15–21], Tb^{3+} [22, 23], and Tm^{3+} [4, 10]. However, a complete crystal field calculation of Eu^{3+} Zeeman-hyperfine structure has not been demonstrated. Terms that are omitted for other ions due to their relatively small contributions become important in the commonly studied $J = 0$ crystal field levels in Eu^{3+} . These are the nuclear quadrupole contribution from the lattice field gradient and the nuclear Zeeman. The qualitative contribution of these terms to the Zeeman-hyperfine structure in Eu^{3+} is well-established [24–27], but accurate estimates of their exact size in different sites have largely been lacking. Here, we implement a crystal field model with all contributions included, and apply the model to three different Eu^{3+} sites: the C_{4v} and C_{3v} sites in CaF_2 , and the C_2 site in $\text{EuCl}_3 \cdot 6\text{H}_2\text{O}$. We also extract spin Hamiltonian parameters from the crystal field fit and discuss how crystal field models can be used to resolve ambiguities in the spin Hamiltonian.

II. THEORETICAL BACKGROUND

A. Crystal field Hamiltonian

Here, we first present the full crystal field Hamiltonian for the $4f$ configuration with expressions for each individual term. Most of these expressions have been covered in detail, [4, 5, 28–30], but we found it important to give all terms in a unified notation.

The complete Hamiltonian appropriate for modeling the $4f^N$ configuration is

$$H = H_{\text{FI}} + H_{\text{CF}} + H_{\text{Z}} + H_{\text{HFS}}. \quad (1)$$

The terms in Eq. (1) represent the free-ion, crystal-field, electronic and nuclear Zeeman, and hyperfine interactions respectively.

The free-ion Hamiltonian H_{FI} can be expressed as [31]

$$\begin{aligned} H_{\text{FI}} = & E_{\text{avg}} + \sum_{k=2,4,6} F^k f_k + \zeta_{4f} A_{\text{SO}} + \alpha L(L+1) \\ & + \beta G(G_2) + \gamma G(R_7) + \sum_{i=2,3,4,6,7,8} T^i t_i \\ & + \sum_{i=0,2,4} M^i m_i + \sum_{i=2,4,6} P^i p_i. \end{aligned} \quad (2)$$

In this equation, E_{avg} describes the spherically symmetric part of the Hamiltonian which shifts the entire configuration, F^k and ζ_{4f} describe the electrostatic and spin-orbit integrals, respectively, and f_k and A_{SO} represent the angular parts of the electrostatic and spin-orbit interactions, respectively. The remainder of the terms are smaller. Interactions with other configurations of the same parity as the $4f$ configuration are described by two-body Trees configuration interaction parameters α , β and γ , where L is the total angular momentum, and $G(G_2)$ and $G(R_7)$ are the Casimir operators [32] for the groups G_2 and R_7 [33]. The three-body interaction parameters T^i and three-body operators t_i are included for systems of more than two electrons and account for couplings of the f^N states to states in higher energy configurations via Coulomb interactions [34]. Finally, two relativistic corrections are included, the Marvin integrals M^i for spin-spin and spin-other-orbit effects [35], and the two-body electrostatically correlated magnetic configuration interaction parameters P^i [36], with m_i and p_i being the associated operators. Methods for calculating matrix elements using reduced matrix elements tabulated by Nielson and Koster [37] have been covered in detail [29]. Mean free-ion parameters have been tabulated for the rare-earth ions [38], however it is necessary to allow E_{avg} , the Slater parameters F^k , and spin orbit parameter ζ_{4f} to vary during fitting to experimental levels as these parameters have the most significant effect on the calculated spectra.

The crystal field Hamiltonian H_{CF} can be written as

$$H_{\text{CF}} = \sum_{k=2,4,6} \sum_{q=-k}^k B_q^k C_q^{(k)}, \quad (3)$$

where B_q^k are the crystal field expansion coefficients, and $C_q^{(k)}$ are spherical tensor operators using Wybourne's normalization of the spherical harmonics Y_{kq} [28]:

$$C_q^{(k)} = \sqrt{\frac{4\pi}{2k+1}} Y_{kq}. \quad (4)$$

The parameters B_q^k are complex, composed of real parameters \mathcal{B}_q^k and \mathcal{B}_{-q}^k such that [39]:

$$B_q^k = \mathcal{B}_q^k + i\mathcal{B}_{-q}^k, \quad (5)$$

$$B_{-q}^k = (-1)^q [\mathcal{B}_q^k - i\mathcal{B}_{-q}^k]. \quad (6)$$

It is for this reason that the parameters \mathcal{B}_q^k with negative q are often referred to as the imaginary crystal field parameters despite taking real values. The number of parameters \mathcal{B}_q^k depends on the point symmetry of the rare earth ion site. Table IV in the Supplementary Materials lists the non-zero parameters for each of the crystallographic point groups.

In the presence of an external magnetic field \mathbf{B} , the Zeeman Hamiltonian H_Z is [24]

$$H_Z = H_{eZ} + H_{nZ}, \quad (7)$$

with

$$H_{eZ} = \mu_B \mathbf{B} \cdot (\mathbf{L} + g_s \mathbf{S}), \quad (8)$$

$$H_{nZ} = -g_n \mu_N \mathbf{B} \cdot \mathbf{I}, \quad (9)$$

where H_{eZ} is the electronic Zeeman interaction and H_{nZ} the nuclear Zeeman interaction. \mathbf{L} and \mathbf{S} are the total electronic orbital and spin angular momentum operators, g_s is the electron spin g -factor, μ_B is the Bohr magneton, μ_N is the nuclear magneton, and g_n is the nuclear g -factor. Matrix elements for these terms are given in Refs. [4, 5].

The calculation of hyperfine structure is treated by a multipole expansion of the interactions between the electronic and nuclear states. Generally, only interactions involving the magnetic dipole moment and electric quadrupole moment are considered, as higher order multipoles have a negligible contribution in comparison [28]. The hyperfine Hamiltonian H_{HFS} is then expressed as

$$H_{\text{HFS}} = H_{\text{MD}} + H_{\text{Q}}, \quad (10)$$

where H_{MD} and H_{Q} are the contributions from magnetic dipole and electric quadrupole moment interactions respectively.

The magnetic dipole contribution is given by [33]

$$H_{\text{MD}} = a_i \sum_i \mathbf{N}_i \cdot \mathbf{I}, \quad (11)$$

$$\mathbf{N}_i = \mathbf{l}_i - \sqrt{10} (\mathbf{sC}^{(2)})_i^{(1)}, \quad (12)$$

where \mathbf{l}_i and \mathbf{s}_i are the orbital and spin angular momentum of the electron i , and \mathbf{I} is the nuclear spin operator. a_i is a constant given by [28]

$$a_i = 2\mu_B g_n \mu_N \frac{\mu_0}{4\pi} (1-R) \langle r_e^{-3} \rangle, \quad (13)$$

where μ_B is the Bohr magneton, μ_0 is the vacuum permeability, R is a shielding factor describing the effect of the induced closed shell quadrupole moment on the $4f$ electrons [25, 40, 41], and $\langle r_e^{-3} \rangle$ is the average inverse-cube radius of the $4f$ orbital. Whilst a_i can be related to physical constants, during crystal field fitting it is treated as a free parameter due to the shielding factor R .

The electric quadrupole contribution arises from the interaction between the nuclear quadrupole moment and

field gradient at the nucleus, which has three sources: the lattice, the $4f$ electrons, and the spherically symmetric closed shells [29]. The latter is included as shielding and antishielding coefficients in the former two terms. Thus, the quadrupole can be written:

$$H_Q = H_Q^{\text{lat}} + H_Q^{4f}, \quad (14)$$

where H_Q^{lat} is the lattice contribution and H_Q^{4f} is the $4f$ contribution. The lattice contribution is given by

$$H_Q^{\text{lat}} = - \sum_{q=-2}^2 (-1)^q \left(\frac{(1-\gamma_\infty)}{(1-\sigma_2) \langle r_e^2 \rangle} B_q^2 \left(r_n^2 (C_n)_q^{(2)} \right) \right), \quad (15)$$

where $(C_n)_q^{(2)}$ is a spherical tensor operator (Eq. (4)) operating on the nuclear wave function, r_n^2 is the nuclear radius, $\langle r_e^2 \rangle$ and is the mean square radius of the $4f$ orbital. γ_∞ is the quadrupole anti-shielding parameter accounting for the effect of the quadrupole moment induced on the closed shells by the nucleus, while σ_2 describes the shielding of the lattice field by the filled $5s$ and $5p$ shells. The $4f$ contribution is given by

$$H_Q^{4f} = \frac{-e^2}{4\pi\epsilon_0} \sum_{q=-2}^2 (-1)^q \left(r_n^2 (C_n)_q^{(2)} \right) \times (1-R) \langle r_e^{-3} \rangle \sum_i (C_{ei})_{-q}^{(2)}, \quad (16)$$

where $(C_{ei})_{-q}^{(2)}$ is a spherical tensor operator (Eq. (4)) operating on the wave function of the electron i , and e and ϵ_0 are the electron charge and vacuum permittivity respectively. Matrix elements for the lattice and $4f$ quadrupole terms are provided in Refs. [4, 5].

In the crystal field model, the quadrupole interactions are parameterized using rank two unit tensor operators \mathbf{U} as

$$H_Q^{\text{lat}} = \sum_{q=-2}^2 N_q^2 (U_n)_q^{(2)}, \quad (17)$$

$$H_Q^{4f} = E_Q \frac{1}{2} \left(\frac{(I+1)(2I+1)(2I+3)}{I(2I-1)} \right)^{\frac{1}{2}} \mathbf{U}_n^{(2)} \cdot \mathbf{U}_e^{(2)}, \quad (18)$$

where $\mathbf{U}_e^{(2)}$ operates on the electronic part of the wave function and $\mathbf{U}_n^{(2)}$ operates on the nuclear part. The strength of the interactions is scaled by the fitted parameters N_q^2 for the lattice contribution and E_Q for the $4f$ contribution. Both parameters can be related to physical constants

$$N_q^2 = \frac{-(1-\gamma_\infty)}{(1-\sigma_2) \langle r_e^2 \rangle} \frac{Q}{2} \left(\frac{(I+1)(2I+1)(2I+3)}{I(2I-1)} \right)^{\frac{1}{2}} B_q^2, \quad (19)$$

$$E_Q = \frac{-e^2 Q}{4\pi\epsilon_0} (1-R) \langle r_e^{-3} \rangle, \quad (20)$$

where the nuclear quadrupole moment Q is introduced through the reduced matrix element

$$\langle I || r_n^2 C_n^{(2)} || I \rangle = \frac{Q}{2} \left(\frac{(I+1)(2I+1)(2I+3)}{I(2I-1)} \right)^{\frac{1}{2}}, \quad (21)$$

However, since the shielding/antishielding factors R , γ_∞ and σ_2 do vary between materials, N_q^2 and E_Q were free fitting parameters in the model bounded by the known ranges of the shielding/antishielding factors [42]. Additionally, due to the dependence of N_q^2 on the crystal field, this parameter was also bounded by the ratio and signs of the B_q^2 parameters.

In summary, the full crystal field Hamiltonian in Eq. (1) for the $4f$ configuration can be expanded as

$$H = H_{FI} + H_{CF} + (H_{eZ} + H_{nZ}) + (H_{MD} + H_Q^{\text{lat}} + H_Q^{4f}), \quad (22)$$

with expressions for each term given above, along with references to tabulations of the corresponding matrix elements in LS coupling. In principle, numerically fitting this equation to a particular rare earth ion requires 49 total parameters for C_1 symmetry, however, in practice, the number of parameters allowed to vary in a fit is generally far smaller, as many of parameters are restricted to the average values or ratios calculated from a number of host crystals.

B. Previous modeling of Zeeman-hyperfine structure

Although most previous crystal field modeling for rare earth crystals has considered only H_{FI} and H_{CF} , several workers have included certain of the hyperfine and Zeeman terms in Eq. (22). However, these calculations have typically omitted the lattice nuclear quadrupole and nuclear Zeeman interactions based on the assumption that these are negligible contributions compared to the magnetic dipole, $4f$ quadrupole, and electronic Zeeman effects. To understand when this assumption may be valid, it is useful to examine relative sizes of the various contributions in different types of electronic states.

For the Kramers doublets in ions such as Er^{3+} , the hyperfine splittings are dominated by the magnetic dipole, with $\sim 90\%$ of the observed structure being attributed to this interaction [12, 43]. This is due to the true doublet states of Kramers ions which directly allow a large first order magnetic dipole contribution. This generally holds true for any of the Kramers ions [44]. Therefore, accurate fits to crystal field levels and hyperfine structure can be achieved by incorporating only the magnetic dipole and $4f$ quadrupole contributions, as has been demonstrated for Er^{3+} in several materials including LiYF_4 [11, 12], YPO_4 [14], and both sites of Y_2SiO_5 [13].

Similar to the Kramers doublets, the non-Kramers doublets and pseudo-doublets are also largely dependent on the magnetic dipole interaction. In true doublets such

as the high symmetry (C_{4v}) $\text{Pr}^{3+}:\text{CaF}_2$ ground state [8], there is again a large first order magnetic dipole term. In pseudo-doublet ground states (two singlets split by only a few cm^{-1}) such as those observed in Ho^{3+} [7, 15, 21] or Tb^{3+} [22, 23], it is the second order magnetic dipole interaction, commonly referred to as the pseudo-quadrupole (see Section III B), that has the largest contribution. Provided the crystal field splitting of the pseudo-doublet ground state is accurately modeled, satisfactory fits to the hyperfine splittings of transitions can be achieved by calculating the magnetic dipole interaction, with the $4f$ quadrupole having only a minor effect on the splittings [15]. Sufficiently accurate splittings of the ground state pseudo-doublet can be achieved by the inclusion of the two-electron correlation crystal field parameters [7], or by manual manipulation of the levels [21]. Hyperfine structure of non-Kramers doublets and pseudo-doublets has been successfully calculated in several hosts, including CaF_2 [7, 8, 15, 23], SrF_2 [8, 23], LiYF_4 [20, 22], KY_3F_{10} [18], CaWO_4 [19], $\text{YAl}_3(\text{BO}_3)_4$ [16], YPO_4 [17], and both sites of Y_2SiO_5 [21].

For non-Kramers singlet states in $J \neq 0$ multiplets, the largest contribution to the hyperfine splittings can vary depending on the magnitude of the splittings to nearby crystal field levels within the multiplet. If this splitting is $> 100 \text{ cm}^{-1}$, the level mixing is typically too small to allow a significant pseudo-quadrupole contribution to the hyperfine structure. In these cases, the largest contribution is the $4f$ quadrupole, but the lattice quadrupole may also need to be considered. For example, hyperfine structure was calculated the $^1D_2(0)$ state of Pr^{3+} in LiYF_4 [9, 10] by including $4f$ quadrupole and pseudo-quadrupole terms, but a 13% discrepancy with experimental data was observed. This is likely due to a significant lattice quadrupole contribution, which was shown to be important in $\text{Pr}^{3+}:\text{La}_2(\text{WO}_4)_3$ [5, 45], where the lattice quadrupole contributed $\sim 25\%$ of the total hyperfine splitting of $^1D_2(0)$.

For non-Kramers singlets with $J = 0$, such as 7F_0 and 5D_0 in Eu^{3+} , the situation is quite different. H_Q^{lat} and H_{nZ} are the dominant sources of the hyperfine splittings as H_{eZ} , H_{MD} and H_Q^{4f} have zero matrix elements for $J = 0$ states. It is only through J -mixing induced by the crystal field that these terms contribute at all. In these cases, an accurate crystal field calculation is important as the magnitudes of the contributions are sensitive to the splittings to nearby multiplets. In summary, the lattice quadrupole contribution is most significant in non-Kramers singlet states, especially those of $J = 0$, and can be ignored in Kramers ions and non-Kramers doublets and pseudo-doublets.

We now turn to the second of the small hyperfine terms, the true nuclear Zeeman term. This is nearly always considered unimportant as the enhancement of the nuclear moment due to the magnetic dipole (the pseudo-nuclear effect, see Section III B) is several orders of magnitude larger than the bare nuclear moment in most situations [46]. However, the true nuclear Zeeman effect be-

comes important in $J = 0$ multiplets, where the pseudo-nuclear term is small, or in cases where the crystal field mixing results in a large pseudo-nuclear Zeeman component in only one direction, such as $\text{Tm}^{3+}:\text{Y}_3\text{Al}_5\text{O}_{12}$ [4].

We finish by highlighting an important point for quantum information applications, where the crystal field models are often used to predict observables dependent on the wave functions output from the model (such as relative transition probabilities), not just the energy levels. To accurately reproduce these observables, Guillot-Noël *et al.* showed that it is important to use the true site symmetry [5], rather than to take the common approach of refining the crystal field parameters of low symmetry sites in slightly higher symmetry (such as C_{2v} for C_2 or C_1). This approach has been widely, and successfully, applied for predictions of crystal field energy level structure, either to reduce the computational complexity or because a lack of data means the lower symmetry crystal field fit is underdetermined. However, it is precisely the mixing caused by the lower symmetry that becomes important for transition probabilities (for instance), so the full symmetry must be used.

Here, we use the full crystal field model and the true site symmetry of three different Eu^{3+} sites to determine quantitative contributions of different terms to the hyperfine splitting and relative oscillator strengths. While the qualitative contributions to Eu^{3+} hyperfine splittings are well known [24, 26, 27, 47], the lack of a full crystal field model has prevented quantitative determination of the relative size of different contributions. This makes Eu^{3+} an excellent test-bed for the full crystal field model.

III. SPIN HAMILTONIAN THEORY

As described above, the first goal of this paper is to provide accurate crystal field models for Eu^{3+} sites. The second goal, addressed in this section, is to provide a direct relationship between the crystal field model and the phenomenological spin Hamiltonian models commonly used in experimental studies of hyperfine structure of individual crystal field levels. The widely used existing expression [48] suitable for other non-Kramers singlet states is inappropriate for the $J = 0$ levels of Eu^{3+} because it ignores J mixing effects. A correct, crystal field derived expression both allows a physical interpretation of the spin Hamiltonian parameters and resolves certain parameter ambiguities that arise when fitting phenomenological models.

A. Phenomenological spin Hamiltonian

We first consider the experimental approach to the spin Hamiltonian, and highlight the ambiguities that exist when fitting this Hamiltonian to data. For an electronic singlet state, the appropriate phenomenological spin Hamiltonian contains operators for the nuclear spin

only:

$$H_{eff} = (\mathbf{B} \cdot \mathbf{Z} \cdot \mathbf{B})\mathbf{1} + \mathbf{B} \cdot \mathbf{M} \cdot \mathbf{I} + \mathbf{I} \cdot \mathbf{Q} \cdot \mathbf{I}, \quad (23)$$

where \mathbf{B} is the magnetic field, \mathbf{I} is the nuclear spin operator, $\mathbf{1}$ is the identity operator, \mathbf{Z} is the quadratic Zeeman tensor, \mathbf{M} the linear Zeeman tensor, and \mathbf{Q} the traceless enhanced quadrupole tensor. These three symmetric tensors are unique to that electronic state, and are only constrained by the site symmetry. The most general form of these tensors (applicable to C_1 symmetry) is:

$$\mathbf{Z} = \mathbf{R}_Z \cdot \begin{bmatrix} Z_x & 0 & 0 \\ 0 & Z_y & 0 \\ 0 & 0 & Z_z \end{bmatrix} \cdot \mathbf{R}_Z^T, \quad (24)$$

$$\mathbf{M} = \mathbf{R}_M \cdot \begin{bmatrix} g_x & 0 & 0 \\ 0 & g_y & 0 \\ 0 & 0 & g_z \end{bmatrix} \cdot \mathbf{R}_M^T, \quad (25)$$

$$\mathbf{Q} = \mathbf{R}_Q \cdot \begin{bmatrix} -E - \frac{1}{3}D & 0 & 0 \\ 0 & E - \frac{1}{3}D & 0 \\ 0 & 0 & \frac{2}{3}D \end{bmatrix} \cdot \mathbf{R}_Q^T, \quad (26)$$

where $\mathbf{R}_i = R(\varphi_i, \theta_i, \psi_i)$ is an Euler rotation matrix. In C_2 symmetry, the lowest symmetry studied here, $\varphi = \theta = 0$ for all tensors when the laboratory frame z is aligned with the C_2 axis. For axial symmetries such as C_{4v} and C_{3v} , all tensors are aligned, $g_x = g_y$, and $E = 0$.

Experimentally, the spin Hamiltonian parameters required for the particular site symmetry are fit to hyperfine splitting data for a variety of magnetic field values, typically obtained using nuclear magnetic resonance, optically detected nuclear magnetic resonance, or Raman heterodyne spectroscopy. Such a fit furnishes a set of non-unique spin Hamiltonian parameters, because the spin Hamiltonian is insensitive to certain transformations. For instance, in C_2 symmetry the Hamiltonian is insensitive to the sign of \mathbf{Z} , \mathbf{M} , \mathbf{Q} , g_z , and D , and the sign of E is ill-defined since it can be reversed by rotating the entire spin Hamiltonian 90° about z .

Further, there are three possible sets of parameters corresponding to different, equivalent choices of the quantization axis of the quadrupole term. Any one set accurately fits the spin Hamiltonian of a single electronic state, but problems arise when trying to calculate parameters that depend on spin Hamiltonians of two different electronic states, such as relative oscillator strengths. The relative optical transition probability P_{ij} of transitions between different hyperfine states in ground (i) and excited (j) levels can be calculated from the overlap of the nuclear wave functions Ψ^n determined from the spin Hamiltonians of the two levels:

$$P_{ij} = |\langle \Psi_{gi}^n | \Psi_{ej}^n \rangle|^2. \quad (27)$$

However, this is only true if the same quadrupole quantization axes have been used for both spin Hamiltonians.

Finally, a further difficulty arises in materials with multiple magnetically inequivalent subsites, which occur in

materials where the rare earth site symmetry is lower than the crystal symmetry. While the spin Hamiltonian of all subsites can be generated from the spin Hamiltonian for one site using the symmetry operations of the crystal, the same base subsite must be correctly chosen for every electronic level. When there is no obvious relationship between spin Hamiltonian parameters in different electronic states, identifying the same subsite can be very difficult. This was seen in $\text{Pr}^{3+}:\text{YAlO}_3$ [49], which has two magnetic subsites related by a C_2 rotation: the fitted spin Hamiltonian parameters for the 7F_0 and 5D_0 levels in [49] are for different subsites.

Additional measurements, such as the relative optical oscillator strength measurements described above, can resolve some but not all of these ambiguities. A crystal field-based spin Hamiltonian, in contrast, can resolve all physically significant spin Hamiltonian parameter ambiguities.

B. Crystal-field-based spin Hamiltonian

The spin Hamiltonian suitable for a non-Kramers singlet state, ignoring J -mixing, is normally taken to be [44, 48]

$$H = -\mathbf{B} \cdot (g_J^2 \mu_B^2 \mathbf{\Lambda}) \cdot \mathbf{B} - \mathbf{B} \cdot (g_n \mu_N \mathbf{1} - 2A_J g_J \mu_B \mathbf{\Lambda}) \cdot \mathbf{I} - \mathbf{I} \cdot (A_J^2 \mathbf{\Lambda} + \mathbf{T}_Q) \cdot \mathbf{I}, \quad (28)$$

where g_J is the Landé g value, and A_J is the hyperfine interaction parameter for that state. The lattice and $4f$ quadrupole contributions are combined into a single true quadrupole term \mathbf{T}_Q and $A_J^2 \mathbf{\Lambda}$ accounts for the pseudo-quadrupole contribution arising from the magnetic dipole interaction. The contributions from other electronic states are encapsulated by the tensor $\mathbf{\Lambda}$ which sums the interaction with all other states in the multiplet:

$$\Lambda_{ij} = \sum_{n=1}^{2J+1} \frac{\langle 0 | J_i | n \rangle \langle n | J_j | 0 \rangle}{E_n - E_0}, \quad (29)$$

with $|0\rangle$ the singlet state of interest.

When dealing with only the hyperfine splittings, the first term of Eq. (28) is ignored, leaving the latter two terms. This form is sufficient when working within a single LSJ state, as the largest contributions to the splittings come from interactions with crystal field levels within the same multiplet. Summation over the electron configurations of a single multiplet allows for many of the interactions to be related to the total angular momentum operator \mathbf{J} , simplifying the form of the spin Hamiltonian; $\mathbf{\Lambda}$ can be used to describe several effects that have the same symmetry despite originating from different physical interactions.

The $J = 0$ levels in Eu^{3+} are an example of the breakdown of the simple J approximation used above: the observed splittings are influenced by J -mixing *between* multiplets through the second order polarization of the $4f$

electrons, pseudo-quadrupole, and pseudo-nuclear Zeeman effects [44]. This prevents the electron configuration summation being used to relate the hyperfine interactions to \mathbf{J} , hence preventing the construction of $\mathbf{\Lambda}$. Instead, we now sum over all possible electronic states $|\Psi\rangle = |\tau LSJM_J\rangle$ of the $4f^N$ configuration for which the matrix elements of $\mathbf{L} + g_s\mathbf{S}$ and \mathbf{N} are non-zero. In this case, it is useful to adopt an approach to the spin Hamiltonian based on interactions described by the crystal field.

The first correction is the pseudo-nuclear Zeeman. In this case we replace $\mathbf{\Lambda}$ by

$$\alpha_{ij} = \sum_{\Psi'} \frac{\langle \Psi | L_i + g_s S_i | \Psi' \rangle \langle \Psi' | N_j | \Psi \rangle}{E_{\Psi'} - E_{\Psi}}, \quad (30)$$

where we consider the mixing of levels by the electronic Zeeman and magnetic dipole interactions. Accounting for the pseudo-nuclear Zeeman effect, the nuclear g -values can be calculated as

$$g_i = g_n \mu_N - 2a_l g_J \mu_B \alpha_{ii} \quad (31)$$

The second correction is the pseudo-quadrupole. Here we replace $\mathbf{\Lambda}$ by

$$P_{ij} = \sum_{\Psi'} \frac{\langle \Psi | N_i | \Psi' \rangle \langle \Psi' | N_j | \Psi \rangle}{E_{\Psi'} - E_{\Psi}}, \quad (32)$$

where we consider the second order contribution from the magnetic dipole interaction. The D and E associated with the pseudo-quadrupole are then given by

$$D_{pq} = a_l^2 \left(\frac{P_{xx} + P_{yy}}{2} - P_{zz} \right), \quad (33)$$

$$E_{pq} = a_l^2 \frac{P_{xx} - P_{yy}}{2}. \quad (34)$$

We also separate the true quadrupole term \mathbf{T}_Q into its two contributions, the lattice \mathbf{T}_{lat} and $4f$ quadrupole \mathbf{T}_{4f} , with forms equivalent to Eq. (26). These then have D and E parameters related to crystal field parameters with

$$D_{lat} = \frac{3N_0^2}{I(2I-1)} \left(\frac{I(2I-1)}{(I+1)(2I+1)(2I+3)} \right)^{\frac{1}{2}}, \quad (35)$$

$$E_{lat} = \sqrt{\frac{2}{3}} \frac{N_0^2}{N_0^2} D_{lat}, \quad (36)$$

for the lattice contribution, and

$$D_{4f} = \frac{3E_Q}{I(2I-1)} \left\langle \psi \left| \sum_i (C_{ei})_0^{(2)} \right| \psi \right\rangle, \quad (37)$$

$$E_{4f} = \sqrt{\frac{2}{3}} \frac{\langle \psi | \sum_i (C_{ei})_2^{(2)} | \psi \rangle}{\langle \psi | \sum_i (C_{ei})_0^{(2)} | \psi \rangle} D_{4f}, \quad (38)$$

for the $4f$ contribution. Here, $|\psi\rangle$ is the wave function for the state in question, accounting for crystal field mixing.

The spin Hamiltonian for any J -mixing dependent system is then given by

$$H = -\mathbf{B} \cdot (g_n \mu_N \mathbf{1} - 2a_l g_J \mu_B \boldsymbol{\alpha}) \cdot \mathbf{I} - \mathbf{I} \cdot (a_l^2 \mathbf{P} + \mathbf{T}_{lat} + \mathbf{T}_{4f}) \cdot \mathbf{I}. \quad (39)$$

Due to the J -mixing dependence of the interactions, the principal axes of the quadrupole terms of Eq. (39) are not necessarily aligned. Instead, each contribution takes the form of Eq. (26) with a unique set of D , E , and Euler angles. The contributions are summed in a common frame to form a total quadrupole tensor, with principal axes given by D_{tot} and E_{tot} , which are not necessarily aligned with the principal axes of any of the individual quadrupole terms. This is in contrast to the nuclear Zeeman tensor which has principal axes that are aligned with the pseudo-nuclear Zeeman contribution as the pure nuclear Zeeman is isotropic.

IV. METHOD

Crystal field calculations were performed using M. F. Reid's F-shell empirical program suite in conjunction with S. Horvath's *pycf* program for low symmetry crystal field parameter fitting [50]. A truncated set of matrix elements was used to reduce computation time following the approach of Carnell *et al.* [51] by first diagonalizing the free-ion Hamiltonian (Eq. 2) using estimates of the free-ion parameters [31], and then using a truncated set of eigenvectors of this diagonalization to generate free-ion and crystal field matrix elements in the intermediate coupled basis. We chose to truncate the matrix elements at 30 free-ion multiplets out of the total 295, resulting in 272 crystal field levels out of the total 3003, with energies up to $\sim 33\,000 \text{ cm}^{-1}$.

For each of the Eu^{3+} centers analyzed, first the free-ion parameters E_{avg} , F^k , and ζ_{4f} along with the crystal field parameters B_q^k required for the site symmetry were fitted to available crystal field energy levels (see Table II in Supplementary Materials). This was done to ensure a satisfactory fit to the crystal field levels before including the hyperfine interactions as adding the nuclear spin means a sixfold increase in the number of states and in the computation time. Next, the crystal field parameters were refitted using the previous parameters as initial values at the same time as fitting the hyperfine parameters a_l , E_Q , and N_q^2 . Whilst the lattice quadrupole parameters N_q^2 have a fixed relationship to the crystal field parameters B_q^2 , theoretically requiring the addition of only a single scaling parameter to account for shielding effects, we instead used free parameter for each q term. This was done to avoid propagating error from the crystal field parameters onto the hyperfine structure, which is discussed in Section VI. Instead, bounds were placed on N_q^2 such that the appropriate sign and approximate relative magnitudes were correctly imposed by the B_q^2 parameters.

For this second round of fitting, the fitting data was the crystal field energy levels, and the hyperfine split-

tings of the 7F_0 state and the 5D_0 state (when available) calculated for 100 magnetic field directions defined on a spiral:

$$\mathbf{B} = \begin{bmatrix} B_0\sqrt{1-t^2}\cos(6\pi t) \\ B_0\sqrt{1-t^2}\sin(6\pi t) \\ B_0t \end{bmatrix} \quad (40)$$

where $B_0 = 400$ mT. We fitted to hyperfine splittings and not absolute frequencies so that any error in the energy of the crystal field levels was not propagated into the hyperfine errors. This way, the hyperfine splittings could still be fitted even if there was a deviation of the crystal field levels away from the experimental values.

In crystal field theory, there always exist sets of crystal field parameters that produce equivalent fits to energy level structure for a given site, but different wave functions and ordering of M_J levels within the multiplets. These sets do not produce the same Zeeman-hyperfine splittings, so this data is needed to constrain the crystal field values. To avoid the fit getting stuck in a local minimum within the crystal field parameter set two methods were employed; a basin-hopping algorithm [52, 53] was used to allow the fit to jump between equivalent sets, and the weighting of the hyperfine and crystal field levels was chosen such that both contributed approximately equally to calculated error.

The fit was accomplished using the multi-Hamiltonian method [50] where a crystal field Hamiltonian is generated for each magnetic field step then diagonalized concurrently. In this method, the parameters can be fitted using experimental data for both the zero-field crystal field levels and Zeeman-hyperfine splittings simultaneously.

Whilst spin Hamiltonian parameters can be calculated from the crystal field parameters as outlined in Section III B, this can become tedious due to the large number of wave function terms that must be considered. Given access to the full crystal field Hamiltonian, it is far easier to extract spin Hamiltonians for the individual electronic states by projecting the crystal field Hamiltonian into the spin Hamiltonian basis, following the method of Ref. [13]. This allows for the direct calculation of the \mathbf{Z} , \mathbf{M} , and \mathbf{Q} parameters, working backward from the full spin Hamiltonian matrix. Additionally, this method preserves sign information, allowing for a unique set of spin Hamiltonian parameters to be determined, including rotations, with all sign ambiguities removed.

V. RESULTS

We studied three different ${}^{151}\text{Eu}^{3+}$ sites of different symmetry for which sufficient crystal field and hyperfine data exists in the literature. These were the C_{4v} and C_{3v} sites in CaF_2 , and the C_2 site in $\text{EuCl}_3 \cdot 6\text{H}_2\text{O}$. Table I lists the fitted crystal field values for each site.

TABLE I. Fitted crystal field parameters (cm^{-1}) for the three Eu^{3+} sites studied here. Where a parameter is blank, that parameter does not occur for the site symmetry.

Parameter	$\text{CaF}_2:C_{4v}$	$\text{CaF}_2:C_{3v}$	$\text{EuCl}_3 \cdot 6\text{H}_2\text{O}$
E_{avg}	64154	64232	63887
F_2	83479	83317	82962
F_4	60024	59405	59580
F_6	42506	42658	42801
ζ	1333	1337	1333
B_0^2	680	2122	70
B_2^2	—	—	$241 + 196i$
B_0^4	-852	1697	-334
B_2^4	—	—	$335 + 465i$
B_3^4	—	-2095	—
B_4^4	-994	—	$-316 - 175i$
B_0^6	1317	-657	700
B_2^6	—	—	$308 - 396i$
B_3^6	—	-913	—
B_4^6	-1311	—	$727 - 432i$
B_6^6	—	1366	$-269 + 175i$
a_l	0.0405	0.0433	0.0386
E_Q	-0.0490	-0.0497	-0.0408
N_0^2	-0.00619	-0.0111	-0.000853
N_2^2	—	—	$-0.00466 - 0.00225i$

A. $\text{Eu}^{3+}:\text{CaF}_2$ C_{4v} Center

In the C_{4v} site of CaF_2 , Eu^{3+} substitutes for Ca^{2+} , with charge compensation arising from an interstitial neighboring F^- ion. There are values in the literature for the Zeeman-hyperfine splittings of the 7F_0 and 5D_0 states [54], the energy levels [55], and the fitted crystal field parameters [55]. Here, we re-fitted the crystal field parameters in the full model using the published experimental energy levels [55]. Fitted crystal field parameters are given in Table I, and experimental and calculated spin Hamiltonian parameters given in Table II. The re-fitted crystal field parameters are within $\sim 10\%$ of the values given in [55]. This small change is expected as our fit gives equal weight to the Zeeman-hyperfine splittings, which are most strongly influenced by the positions of the crystal field levels in the 7F_1 and 7F_2 multiplets. Figure 1 shows the comparison between experimental and fitted hyperfine structure for the 7F_0 and 5D_0 states. The Zeeman structure is displayed for fields in a circle in the xz plane:

$$\mathbf{B} = \begin{bmatrix} B_0 \cos(2\pi t) \\ B_0 \sin(2\pi t) \end{bmatrix}. \quad (41)$$

The C_{4v} site of CaF_2 is a good illustration of the established qualitative understanding of hyperfine structure in the $J = 0$ levels of Eu^{3+} , which we briefly summarize. The zero field hyperfine structure in these levels arises from the combination of the lattice quadrupole interaction and effects due to the admixture of $J = 2$ crystal

TABLE II. Spin Hamiltonian parameters for the $^{151}\text{Eu}^{3+}:\text{CaF}_2$ C_{4v} site calculated from crystal field fitting compared to experimental spin Hamiltonian parameters [54]. In that work, signs of the g -values could not be determined, so we list them with ‘ \pm ’ here.

	7F_0		5D_0	
	Calc.	Exp.	Calc.	Exp.
D_{pq} (MHz)	0.198	—	0.00265	—
D_{4f} (MHz)	10.968	—	0.661	—
D_{lat} (MHz)	-13.562	—	-13.708	—
D_{tot} (MHz)	-2.395	-2.415	-13.045	-13.05
g_x (MHz T $^{-1}$)	-0.936	± 0.212	9.646	—
g_y (MHz T $^{-1}$)	-0.936	± 0.212	9.646	—
g_z (MHz T $^{-1}$)	5.075	± 4.657	9.761	—

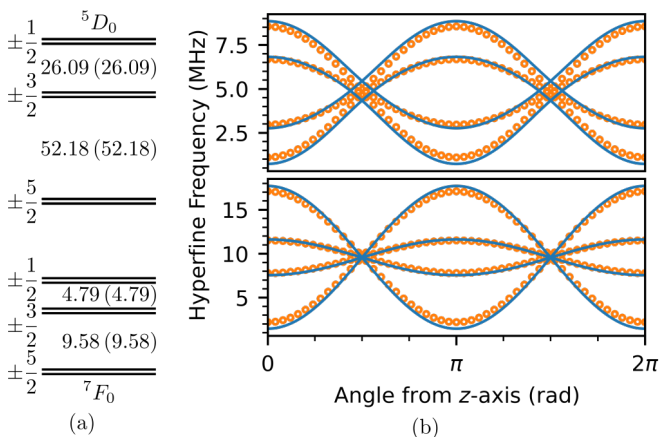


FIG. 1. (a) Calculated zero field splittings of the $\text{Eu}^{3+}:\text{CaF}_2$ C_{4v} site with experimental splittings given in brackets. (b) Calculated (blue) and experimental (orange) Zeeman splittings of the 7F_0 $\pm\frac{3}{2} \rightarrow \pm\frac{1}{2}$ (top) and $\pm\frac{5}{2} \rightarrow \pm\frac{3}{2}$ (bottom) hyperfine transitions for a magnetic field of 400 mT rotated in the xz plane. Experimental points are calculated from published experimental spin Hamiltonian parameters [54].

field levels into the 7F_0 and 5D_0 wave functions by the crystal field [24, 56]. This mixing is only large in the ground state as the separation of the $J = 2$ levels (the 7F_2 multiplet) is much smaller than in the excited state (the 5D_2 multiplet). This is clear from the fitted wave functions of the 7F_0 and 5D_0 states (ignoring contributions $< 1\%$):

$$\Psi({}^7F_0) = -0.99 |{}^7F_0, 0\rangle + 0.12 |{}^7F_2, 0\rangle, \quad (42)$$

$$\Psi({}^5D_0) = +1.00 |{}^5D_0, 0\rangle. \quad (43)$$

This mixing gives rise to the $4f$ contribution to the spin Hamiltonian quadrupole term, which is only significant in the 7F_0 state. However, since this term is of opposite sign to the lattice quadrupole term, the result is smaller quadrupole tensor in the 7F_0 state.

For this C_4 site, Fig. 1(a) shows that the agreement between experimental and calculated zero field splittings is excellent. The quantitative parameter results (Table II)

also agree well with the qualitative description above. In the 5D_0 state, the lattice contribution to the quadrupole term is over 95%, whereas in the ground state, roughly equal magnitude, opposite sign $4f$ and lattice contributions result in a quadrupole $< 20\%$ of the excited state. In both states, the pseudo-quadrupole contribution to the quadrupole tensor is near negligible. This term arises from interactions with $\Delta M_J = 0, 1$ levels. For $J \neq 0$ states, the pseudo-quadrupole can be significant since these interactions exist within the multiplet. However, for the $J = 0$ levels, the large separations to the interacting 7F_1 and 5D_1 states largely suppress this term.

While the zero field structure of the $J = 0$ levels is determined by mixing with $J = 2$ multiplets, the Zeeman structure in a magnetic field is understood to be determined by the small amount of mixing with the $J = 1$ multiplets. This mixing allows for non-zero matrix elements for the electronic Zeeman interaction between the nuclear states [46]. While in $J \neq 0$ states this pseudo-nuclear Zeeman term typically entirely dominates the bare moment, the large spacing to the $J = 1$ multiplets means the contribution is much smaller for $J = 0$ states [24]. Again, the contribution is typically only significant in the 7F_0 state due to the smaller separation to 7F_1 , and again, it is of similar size and opposite sign to that of the true nuclear Zeeman effect. This means g -values are typically smaller in the 7F_0 state compared to the 5D_0 state. Depending on the proximity of the 7F_1 levels, the pseudo-nuclear Zeeman contribution can be large enough that the sign of the g -values is reversed relative to the bare nuclear magnetic moment.

We see from Fig. 1(b) and Table II that, as expected, in 5D_0 the predicted g -values are only slightly reduced from the bare moment of 10.58 MHz T^{-1} by the small amount of mixing with 5D_1 . In the ground state, the g -values are substantially reduced by the mixing. The predicted values in this level do differ from the experimental numbers. This discrepancy can be attributed to the $\approx 5\%$ deviation of the calculated crystal field splittings of the 7F_1 from the experimental values, since the pseudo-nuclear term is highly sensitive to the separation of the 7F_1 and 7F_0 levels. Nevertheless, the agreement is sufficient to resolve the sign ambiguity in the experimental g values: $g_{x,y}$ is negative, and g_z is positive.

B. $\text{Eu}^{3+}:\text{CaF}_2:\text{O}^{2-}$ C_{3v} Center

In the C_{3v} site of CaF_2 , denoted the G1 center, Eu^{3+} substitutes for Ca^{2+} with charge compensation arising from a substitutional O^{2-} in a neighboring F^- site. Zeeman-hyperfine splittings for this site are available for both the 7F_0 ground and 5D_0 excited states [27, 42, 57–60], but despite these extensive hyperfine studies, the observed crystal field levels are restricted to few 7F_J and 5D_J multiplets [27]. Fitting a set of crystal field parameters to the available energy levels is further complicated by the very strong crystal field caused by the nearby oxy-

gen atom [57] which makes assignment of the 7F_1 and 7F_2 levels difficult [27, 57]. As there has been no prior crystal field fits to the G1 center and the ordering of the ${}^7F_{1,2}$ levels is unknown, we estimated a set of initial crystal field parameters by hand using the 5D_1 and 5D_2 splittings. This set was then refined by fitting to all of the available crystal field and Zeeman-hyperfine data for the site. The ordering of the 7F_1 and 7F_2 levels could then be inferred from the crystal field calculation, demonstrating that the unusually large crystal field causes an overlap of the 7F_1 and 7F_2 multiplets. Fitted crystal field parameters are given in Table I, and experimental and calculated spin Hamiltonian parameters given in Table III. Figure 2 demonstrates the very good agreement between fitted and experimental splittings, with Zeeman structure calculated using Eq. (41).

TABLE III. Spin Hamiltonian parameters for the ${}^{151}\text{Eu}^{3+}:\text{CaF}_2$ C_{3v} site calculated from crystal field fitting compared to experimental spin Hamiltonian parameters [60].

	7F_0		5D_0	
	Calc.	Exp.	Calc.	Exp.
D_{pq} (MHz)	0.610	—	0.008 09	—
D_{4f} (MHz)	31.988	—	2.170	—
D_{lat} (MHz)	-24.344	—	-24.573	—
D_{tot} (MHz)	8.256	8.26	-22.395	-22.23
g_x (MHz T $^{-1}$)	-9.658	-8.998	9.504	9.527
g_y (MHz T $^{-1}$)	-9.658	-8.998	9.504	9.527
g_z (MHz T $^{-1}$)	8.948	9.739	9.751	10.056

Unlike the C_{4v} center, the C_{3v} center does not conform well to the normal picture for $J = 0$ energy level structure because the unusually large crystal field causes considerable mixing between multiplets. In the 5D_0 state the quadrupole interaction $D = -22.395$ MHz is still primarily due to the lattice quadrupole $D_{lat} = -24.573$ MHz, but the contribution from the $4f$ quadrupole $D_{4f} = 2.170$ MHz is double that for the C_{4v} center. This is due to the large $B_0^2 = 2122$ cm $^{-1}$ term mixing the 5D_0 with the 5D_2 state despite these multiplets being separated by ≈ 4000 cm $^{-1}$. The calculated wave functions

$$\Psi({}^7F_0) = +0.92 |{}^7F_0, 0\rangle - 0.35 |{}^7F_2, 0\rangle + 0.11 |{}^7F_4, 0\rangle \\ + 0.10 |{}^7F_4, -3\rangle - 0.10 |{}^7F_4, 3\rangle, \quad (44)$$

$$\Psi({}^5D_0) = -1.00 |{}^5D_0, 0\rangle + 0.04 |{}^5D_2, 0\rangle, \quad (45)$$

demonstrate the considerable mixing compared to the C_{4v} site.

In the 7F multiplet, the crystal field splittings of the 7F_1 and the 7F_2 states generated by the B_0^2 and B_q^4 terms are so large that, as described above, the multiplets are no longer separated and the ordering of states is not obvious. In particular, a doublet state of 7F_2 at 758 cm $^{-1}$ is lower in energy compared to the singlet state of 7F_1 at 865 cm $^{-1}$ (see Supplementary Material Table II). The low lying 7F_2 mixes strongly with 7F_0 resulting in

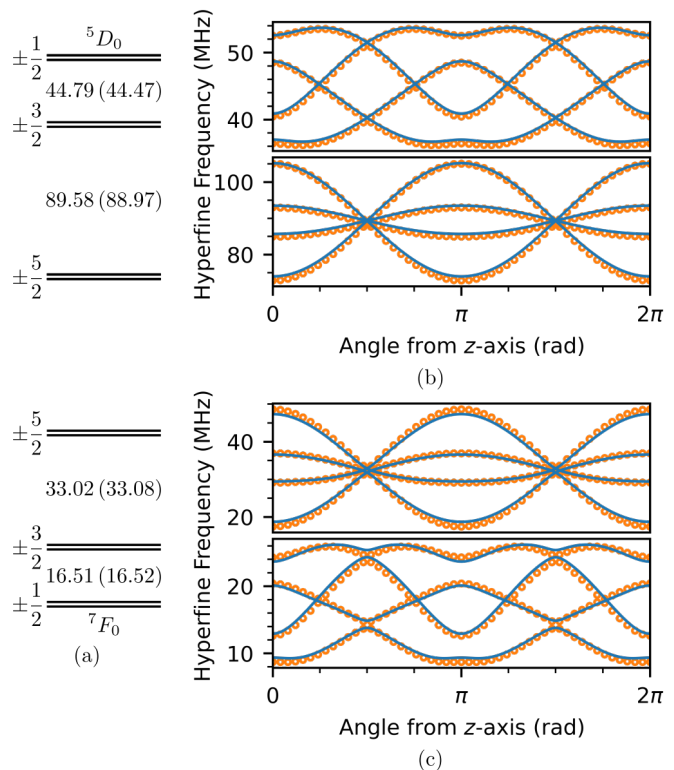


FIG. 2. (a) Calculated zero field splittings of the $\text{Eu}^{3+}:\text{CaF}_2$ C_{3v} site with experimental splittings given in brackets. (b) Calculated (blue) and experimental (orange) Zeeman splittings of the 5D_0 $\pm\frac{3}{2} \rightarrow \pm\frac{1}{2}$ (top) and $\pm\frac{5}{2} \rightarrow \pm\frac{3}{2}$ (bottom) hyperfine transitions for a magnetic field of 400 mT rotated in the $x-z$ plane. (c) Calculated (blue) and experimental (orange) Zeeman splittings of the 7F_0 $\pm\frac{3}{2} \rightarrow \pm\frac{5}{2}$ (top) and $\pm\frac{1}{2} \rightarrow \pm\frac{3}{2}$ (bottom) hyperfine transitions for a magnetic field of 400 mT rotated in the xz plane. Experimental points are calculated from published experimental spin Hamiltonian parameters [60].

a large $4f$ quadrupole contribution $D_{4f} = 31.988$ MHz. This is larger than the lattice quadrupole contribution $D_{lat} = -24.344$ MHz, resulting in a total quadrupole interaction of $D_{tot} = 8.256$ MHz. This reversal of the sign of the quadrupole interaction results in a reversal of the ordering of the nuclear spin states compared to the 5D_0 state.

The g -values of the C_{3v} site do follow a similar pattern to the C_{4v} case. In the excited state, the g -values are only slightly reduced from the bare moment with good agreement between calculation and experiment. Despite the strong crystal field, the splittings between the 5D_0 and 5D_1 states are still large. The influence of the large crystal field is seen more strongly in the ground state. The large splitting within the 7F_1 state pushes the $M_J = \pm 1$ doublet far closer to the 7F_0 state. The resulting large mixing via the magnetic dipole interaction results in a pseudo-nuclear Zeeman effect almost twice the size of the bare moment in the x and y directions. Conversely, since the 7F_1 singlet state is pushed up, the z component of the

pseudo-nuclear Zeeman effect is small ($< 2 \text{ MHz T}^{-1}$) as it arises from mixing with this term. The result is $g_{x,y}$ and g_z values of similar magnitude but opposite sign, agreeing well with the experimental values. Differences in the calculated and experimental 7F_0 g -values are due to inaccuracies in the fitted crystal field levels as the mixing of states is proportional to the splitting as evidenced in Eq. (30).

Previous works have attempted to explain the large pseudo-nuclear Zeeman contribution observed in 7F_0 of the C_{3v} center [27, 60]. This was done without the use a crystal field calculation and it was thought that J -mixing of 7F_2 into 7F_0 would not exceed 1%. Based on this assumption it was concluded that J -mixing could not explain the observed deviations of the electronic Zeeman and magnetic dipole matrix elements from their free-ion values. However, by performing a complete crystal field calculation we have been able to show that J -mixing is far larger than previously thought, close to 13%, which is sufficient to explain the observed pseudo-nuclear Zeeman effect.

C. $\text{EuCl}_3 \cdot 6\text{H}_2\text{O}$ C_2 Center

$\text{EuCl}_3 \cdot 6\text{H}_2\text{O}$ is a stoichiometric crystal in which the Eu^{3+} ion occupies a single site of C_2 symmetry. Several papers over many years have studied the electronic and Zeeman-hyperfine structure [61–67], and it has more recently been investigated for quantum information applications [68–70].

The non-axial site symmetry means that additional crystal field terms must be included: 15 crystal field parameters compared to the 5 (6) for the C_{4v} (C_{3v}) sites. The large number of crystal field parameters caused previous workers to fit the $\text{EuCl}_3 \cdot 6\text{H}_2\text{O}$ crystal field in the higher C_{2v} symmetry [62], but it is precisely the additional crystal field terms that generate the correctly shaped spin Hamiltonian quadrupole and Zeeman tensors. The quadrupole and Zeeman tensors arising from each of the interactions described in Section III B are no longer axial, and the principal axes of these tensors need only coincide along the C_2 direction. Here, we use a selection of the energy levels from Ref. [62] along with some new 7F_J levels determined from fluorescence measurements to fit the site (see Supplementary Materials Table II) using C_2 symmetry and the method described in Section IV. Fitted crystal field parameters are given in Table I, and experimental and calculated spin Hamiltonian parameters given in Table IV. The fitted crystal field parameters are notably different to the those of Ref. [62]. This is due to a combination of the lowering of symmetry from C_{2v} to C_2 and the use of different fixed free-ion parameters. Despite the low symmetry, the agreement between experimental and calculated hyperfine splittings is excellent, as shown in Fig. 3. To display the Zeeman splitting in this non-axial site, we have calculated the structure for the magnetic field spiral in Eq. (40).

TABLE IV. ${}^{151}\text{EuCl}_3 \cdot 6\text{H}_2\text{O}$ spin Hamiltonian parameters calculated from crystal field fitting compared to experimental spin Hamiltonian parameters [68]. Note that we have transformed the spin Hamiltonian parameters of Ref. [68] into the standard electron paramagnetic formalism: the zyz Euler rotation convention, Eq. (A.1). Further, we have chosen the opposite set of equivalent spin Hamiltonian E , g_x and g_y parameters to match the crystal field fit as described in the text.

	7F_0		5D_0	
	Calc.	Exp.	Calc.	Exp.
D_{pq} (MHz)	0.0550	—	0.000 239	—
E_{pq} (MHz)	0.0938	—	0.000 725	—
γ_{pq} ($^\circ$)	-68.33	—	-68.33	—
D_{4f} (MHz)	2.109	—	0.0497	—
E_{4f} (MHz)	4.275	—	0.199	—
γ_{4f} ($^\circ$)	-68.01	—	-68.01	—
D_{lat} (MHz)	-1.866	—	-1.875	—
E_{lat} (MHz)	9.263	—	9.284	—
γ_{lat} ($^\circ$)	12.89	—	12.89	—
D_{tot} (MHz)	0.297 18	0.356 92	-1.825 29	-1.858 68
E_{tot} (MHz)	5.290 24	5.290 26	9.089 41	9.085 95
$\gamma_{Q_{tot}}$ ($^\circ$)	5.43	2.93	12.76	13.22
g_x (MHz T^{-1})	4.115	± 4.029	9.690	9.666
g_y (MHz T^{-1})	-1.723	∓ 1.504	9.647	9.293
g_z (MHz T^{-1})	2.857	3.006	9.686	10.025
γ_M ($^\circ$)	21.81	22.69	19.30	3.1

Again, the excited state quadrupole is dominated by the lattice term, where the additional parameter E accounts for the asymmetry of this non-axial site. The calculated wave functions

$$\Psi({}^7F_0) = (-0.11 - 0.99i) |{}^7F_0, 0\rangle + (0.05 + 0.04i) |{}^7F_2, 2\rangle + (-0.04 + 0.05i) |{}^7F_2, -2\rangle, \quad (46)$$

$$\Psi({}^5D_0) = (-0.34 - 0.94i) |{}^5D_0, 0\rangle, \quad (47)$$

show the strong mixing of the $M_J = \pm 2$ 7F_2 levels into 7F_0 due to the large B_2^2 crystal field parameter. Similarly, there is no mixing of the $M_J = 0$ 7F_2 level into 7F_0 by the much weaker B_0^2 crystal field parameter. As the rank two crystal field parameters are directly related to D and E , this explains the large asymmetry of the spin Hamiltonian quadrupole contributions. There is close agreement between the experimental and calculated values for both the principal axes values and orientation of the tensor. The ground state has comparable $4f$ and lattice quadrupole contributions. These two terms have different orientations of the principle axes, leading to the overall quadrupole tensor in the ground state being misaligned from the excited state by 10° , in reproducing the rotation seen in the experimental data. The fit also resolved the ambiguity in the sign of E : as described in section III B, in a C_2 site the sign of E is poorly defined in a spin Hamiltonian model because a reversal of sign can be compensated for by rotating the M tensor to redefine the orientation of the x and y axes. However,

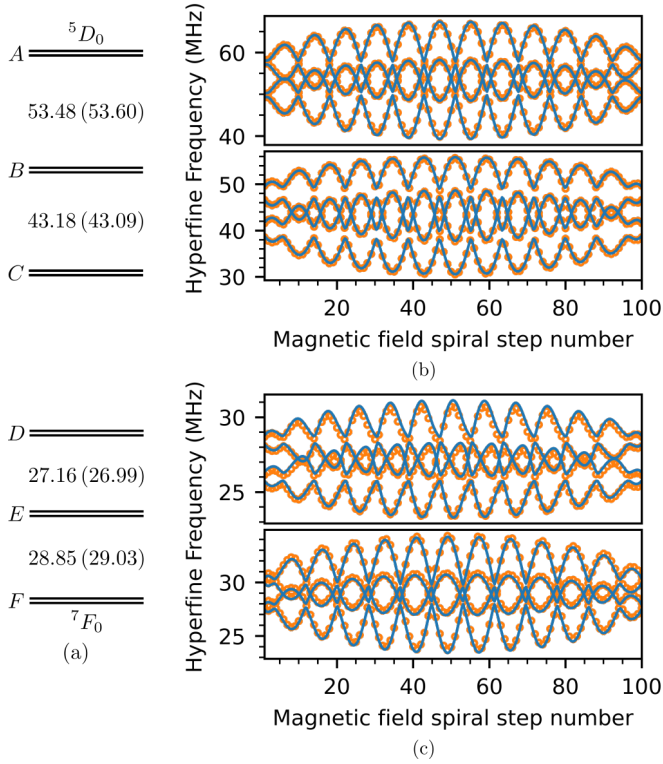


FIG. 3. (a) Calculated zero field splittings of the $\text{EuCl}_3 \cdot 6\text{H}_2\text{O}$ C_2 site with experimental splittings given in brackets. (b) Calculated (blue) and experimental (orange) Zeeman splittings of the 5D_0 $B \rightarrow A$ (top) and $C \rightarrow B$ (bottom) hyperfine transitions for a magnetic field spiral of 400 mT. (c) Calculated (blue) and experimental (orange) Zeeman splittings of the 7F_0 $E \rightarrow D$ (top) and $F \rightarrow E$ (bottom) hyperfine transitions for a magnetic field spiral of 400 mT. Experimental points are calculated from published experimental spin Hamiltonian parameters [68].

the sign of E has physical significance in the crystal field model, and the fit shows that, indeed, the sign of E is negative and the experimental spin Hamiltonian parameters need to be transformed $E \rightarrow -E$, $(g_x, g_y) \rightarrow (g_y, g_x)$, $\gamma \rightarrow \gamma \pm 90^\circ$.

The excited state g -values are again, only slightly reduced from the bare moment. The larger, 10° , discrepancy with the experimental orientation of the Zeeman tensor is unsurprising: given the tensor is nearly isotropic, its orientation is not well defined in either the experimental data or the theoretical calculation. In the ground state, the agreement between experimental data and calculation is close, with the non-axial symmetry giving rise to three unique g -values. From the point of view of the crystal field, this occurs because the additional crystal field parameters split the $M_J = \pm 1$ doublet. The matrix elements of $L_x + 2S_x$ and N_x are large between 7F_0 and the $M_J = +1$ singlet of 7F_1 , and the matrix elements of $L_y + 2S_y$ and N_y are large between 7F_0 and the $M_J = -1$ singlet of 7F_1 . As the $M_J = -1$ singlet is the lowest lying 7F_1 state with a gap of 301 cm^{-1} , the

pseudo-nuclear contribution is largest for fields applied in the y direction, resulting in a large negative contribution to the g -value, sufficient to reverse the sign of the term. Similarly, the smaller x contribution from the $M_J = +1$ singlet 428 cm^{-1} away results in a g_x value closer to the bare moment, with g_z taking a value between these two extremes. Previous work [68] was only able to determine that g_x and g_y had opposite signs; this fit resolves this sign ambiguity.

The Zeeman-hyperfine splittings were also calculated for ${}^{153}\text{Eu}^{3+}$ by scaling the the electric quadrupole moment Q and the nuclear magnetic moment g_n by the ${}^{153}\text{Eu}/{}^{151}\text{Eu}$ ratio, 2.56 and 0.43 respectively [71]. This is not sufficient to match the experimental hyperfine structure, since there is an isotope shift in the crystal field levels which slightly $\mathcal{O}(1\%)$ alters the electronic contributions to the hyperfine levels. This shift is $\sim 220 \text{ MHz}$ on the ${}^7F_0 \rightarrow {}^5D_0$ transition but can be expected to be much larger on $J \neq 0$ transitions. To account for these differences, we fine-tuned the full set of crystal field parameters to obtain the fitted values in Table V.

TABLE V. ${}^{153}\text{EuCl}_3 \cdot 6\text{H}_2\text{O}$ spin Hamiltonian parameters calculated from crystal field fitting compared to experimental spin Hamiltonian parameters [68]. Note that we have transformed the spin Hamiltonian parameters of Ref. [68] into the standard electron paramagnetic formalism: the zyz Euler rotation convention, Eq. (A.1). Further, we have chosen the opposite set of equivalent spin Hamiltonian E , g_x and g_y parameters to match the crystal field fit as described in the text.

	7F_0		5D_0	
	Calc.	Exp.	Calc.	Exp.
D_{tot} (MHz)	0.813 097	0.791 815	-4.815 367	-4.80
E_{tot} (MHz)	13.648 917	13.660 932	23.209 892	23.21
γ_{Qtot} ($^\circ$)	3.21	2.93	12.19	13.22
g_x (MHz T^{-1})	1.878	± 1.794	4.315	4.269
g_y (MHz T^{-1})	-0.422	∓ 0.673	4.298	4.105
g_z (MHz T^{-1})	1.381	1.359	4.315	4.428
γ_M ($^\circ$)	23.08	22.69	20.47	3.1

We also calculated relative oscillator strengths using Eq. (27) (Table VI) for transitions between the 7F_0 and 5D_0 hyperfine levels to determine how well the crystal field model was reproducing the nuclear spin wave functions. Since experimental oscillator strengths are not directly available, we instead compared the excitation spectrum these values generate for the ${}^7F_0 \rightarrow {}^5D_0$ transition with the experimental spectrum for $\text{Eu}^{35}\text{Cl}_3 \cdot 6\text{H}_2\text{O}$ in Fig. 4. The simulated spectrum has only three free parameters: the overall amplitude, the isotope shift (which is too small to be accurately reproduced by the crystal field model), and a parameter accounting for absorption. Given this, the very good agreement confirms the calculated oscillator strengths are accurate.

TABLE VI. Oscillator strengths of the $\text{EuCl}_3 \cdot 6\text{H}_2\text{O}$ ${}^7F_0 \rightarrow {}^5D_0$ nuclear state transitions. State labels follow those of Fig. 3. Calculated values are given by the overlap of the crystal field nuclear wave functions and experimental values are taken from [68].

	${}^{151}\text{Eu}^{3+}$		${}^{153}\text{Eu}^{3+}$	
	Calc.	Exp.	Calc.	Exp.
$F \rightarrow C$	0.9608	0.9300	0.9446	0.9302
$F \rightarrow B$	0.0341	0.0608	0.0483	0.0609
$F \rightarrow A$	0.0050	0.0091	0.0071	0.0089
$E \rightarrow C$	0.0378	0.0687	0.0541	0.0686
$E \rightarrow B$	0.9322	0.8766	0.9031	0.8771
$E \rightarrow A$	0.0299	0.0547	0.0428	0.0544
$D \rightarrow C$	0.0013	0.0013	0.0013	0.0013
$D \rightarrow B$	0.0336	0.0626	0.0486	0.0620
$D \rightarrow A$	0.9650	0.9362	0.9501	0.9367

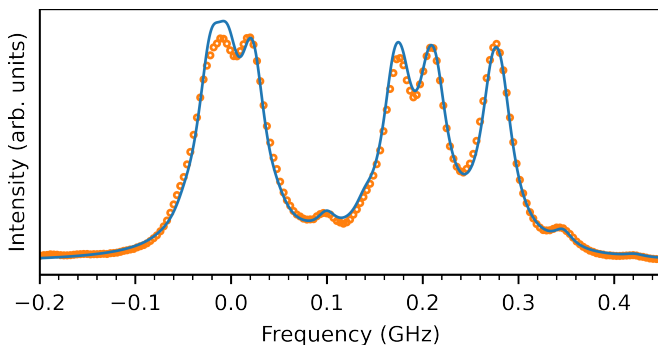


FIG. 4. Simulated and experimental spectra of the ${}^7F_0 \rightarrow {}^5D_0$ nuclear state transitions of ${}^{151}\text{Eu}^{3+}$ and ${}^{153}\text{Eu}^{3+}$ in $\text{EuCl}_3 \cdot 6\text{H}_2\text{O}$. Simulated spectra was calculated using the function $\Gamma(f) = A_0\alpha(f)e^{-\alpha(f)A_1}$ which accounts for absorption of the light in this optically thick sample before reaching the point in the crystal from which emission was collected. We used a Lorentzian line shape α with FWHM line width 0.0122 GHz, and an ${}^{153}\text{Eu}^{3+}$ transition offset of 0.220 GHz.

VI. DISCUSSION

We have shown crystal field theory can be used to accurately calculate Zeeman-hyperfine splittings of the $J = 0$ levels in several different Eu^{3+} as long as the nuclear Zeeman and lattice electric quadrupole terms are included in the calculation. In particular, the lattice contribution to the nuclear quadrupole can be accurately calculated as shown by the 5D_0 splittings in each material, including calculating the rotation about the symmetry axis (in low symmetry) for both the lattice and $4f$ contributions. The crystal field mixing of the 7F_2 and 7F_1 levels into 7F_0 is also well reproduced, allowing accurate determination of the hyperfine structure of this state. In the C_{3v} case we showed that the large deviation of the magnetic dipole and electronic Zeeman matrix elements from their free-ion values [60] is indeed due to an extraordinarily large J -mixing of the 7F_2 and 7F_4 levels into 7F_0 , resolving an

open question in the literature.

It is perhaps surprising how well the model fit the hyperfine structure of each material given, in some cases, how few crystal field levels were available to constrain the fits. In fact, this is the result of a unusual property of the low lying levels in Eu^{3+} : certain crystal field levels have reduced matrix elements $\langle \Psi || U^{(k)} || \Psi \rangle$ which are large for particular k -values and small or non-zero for all other k , allowing those levels to be used to constrain the corresponding crystal field parameter. In Eu^{3+} , 7F_1 is sensitive to B_q^2 , 7F_2 is sensitive to B_q^4 , and ${}^7F_3/{}^7F_4$ are sensitive to B_q^6 , along with 5L_6 to a lesser extent. Whilst there are similar relationships between parameters and individual multiplets and crystal field parameters in other ions (see Ref. [38] for a full list), Eu^{3+} is particular as these special levels are low-lying, so are readily observed in fluorescence spectra of the 5D_0 level. Further, their assignment is rarely ambiguous due to the true singlet nature of 7F_0 and 5D_0 levels, and the large separations 7F_J and 5D_J levels. It is only in particularly unusual cases such as the $\text{CaF}_2 C_{3v}$ site that 7F multiplets overlap. For these reasons, Eu^{3+} might be a good dopant choice when trying to work out the crystal field fitting parameters of a new host material: since parameters vary only slowly across the rare earth series [31] parameters from Eu^{3+} could be used as an initial guess for other rare earth dopants for which assigning observed energy levels is more difficult.

We have emphasized, and demonstrated, that crystal field fits can resolve spin Hamiltonian ambiguities. However, this requires considerable care to be taken during the fitting process, because there are ambiguities in the crystal field fit itself when fitting to only the energies of crystal field levels. There are two types of ambiguity that manifest in crystal field fitting [72, 73]. The first are rotations of the crystal field parameters about the symmetry axis, which occur in centers with imaginary components. The rotational ambiguity arises when the relationship between the crystal field and the experimental crystallographic axes is unknown. It is only by constraining the crystal field parameters through measurements that depend on the true orientation of the crystal, such as Zeeman splittings, that we can resolve this ambiguity. The second ambiguity is complete re-orientations of the symmetry axis which can yield as many as six numerically equivalent crystal field parameter sets [73]. This is typically only an issue at orthorhombic and lower symmetries [72, 74] with multiple non-zero crystal field parameters of every rank. Whilst the the calculated splittings are equivalent for these different sets, the calculated wave functions will differ. Therefore, it is possible to determine the correct set of crystal field parameters by comparing wave function dependent quantities, such as oscillator strengths and Zeeman splittings, to experimental values.

In Eu^{3+} , wave function-dependent information that can be obtained with relative ease. This includes the ordering of the ${}^7F_1 M_J$ levels, and the ordering of the

5D_0 M_I hyperfine states at zero-field. In high symmetry where the only non-zero rank two crystal field parameter is B_0^2 , the 5D_0 hyperfine state ordering is sufficient due to the relationship between the splittings and the lattice quadrupole (Eq. (19)). However, in lower symmetry the introduction of additional B_q^2 parameters means there is insufficient information from just this ordering, and knowledge of the ordering of the 7F_1 levels is needed as well. This can be achieved by measuring the polarized absorption or fluorescence of the ${}^7F_1 \longleftrightarrow {}^5D_0$ transition, or by measuring the 7F_0 nuclear Zeeman g -values. Once the ordering of the 7F_1 levels is known, these can be used to determine the sign and magnitudes of B_q^2 as there is a straightforward relationship between the ordering of the states and the parameters [38]. Restricting the rank two parameters to a single set then restricts the other crystal field parameters. Solving the crystal field parameters sets ambiguities simultaneously solves the spin Hamiltonian sign ambiguities.

One problem with fitting a crystal field model to Eu^{3+} is that several multiplets are poorly simulated by the standard one-electron crystal field model we have used here, the 5D_J multiplets being an example [75]. This frequently results in incorrectly predicted orderings and splittings of the 5D_J states, as well as a change in the free-ion parameters F_k , artificially pushing the 7F_J states down in energy. This effect can be observed in the $\text{EuCl}_3 \cdot 6\text{H}_2\text{O}$ fitting (Supplementary Materials Table II) where the calculated 7F_0 and the 7F_1 levels are significantly lower in energy than the experimental values. To remove the discrepancy in calculated splittings it is necessary to extend the crystal field calculation to account for the effects of electron correlation on the anisotropic crystal field interactions [38]. However, it is typically impractical to include this two-electron crystal field perturbation, referred to as the correlation crystal field, due to the large number of additional parameters required; 637 for the lowest site symmetry [76]. Therefore, effects that would otherwise be accounted for by the correlation crystal field are instead absorbed by the single-electron crystal field. This results in crystal field parameters that are not necessarily a true representation of the crystal field potential.

It is for this reason that we chose to give our model more free parameters than apparently necessary. In our modeling, the lattice quadrupole effect should have a fixed dependency on the single-electron crystal field as shown by Eq. (19). However, to avoid propagating the error in the single-electron crystal field parameters onto the hyperfine structure, the lattice quadrupole parameters N_q^2 were allowed to vary semi-independently of B_q^k . In this way, the N_q^2 parameters are more representative of the true crystal field than the B_q^2 parameters. This ensures a satisfactory fit to both the hyperfine and crystal field structure, whilst maintaining consistency between the crystal field and quadrupole parameters.

VII. CONCLUSIONS

We have calculated Zeeman-hyperfine splittings of Eu^{3+} in three crystallographic centers, the C_{4v} and C_{3v} sites of CaF_2 as well as the C_2 site of $\text{EuCl}_3 \cdot 6\text{H}_2\text{O}$, using a complete crystal field model, with excellent agreement between experimental and calculated values. This was achieved by including the generally omitted lattice quadrupole interaction and nuclear Zeeman interaction, which are important for accurate calculations of hyperfine splittings for non-Kramers singlet states. We have also demonstrated accurate crystal field calculations of oscillator strengths in low symmetry (C_2) by using all parameters required for the exact symmetry of the site.

Appendix

The zyz Euler rotation convention used is given by

$$R(\varphi, \theta, \psi) = \begin{bmatrix} \cos \varphi & \sin \varphi & 0 \\ -\sin \varphi & \cos \varphi & 0 \\ 0 & 0 & 1 \end{bmatrix} \times \begin{bmatrix} \cos \theta & 0 & -\sin \theta \\ 0 & 1 & 0 \\ \sin \theta & 0 & \cos \theta \end{bmatrix} \\ \times \begin{bmatrix} \cos \psi & \sin \psi & 0 \\ -\sin \psi & \cos \psi & 0 \\ 0 & 0 & 1 \end{bmatrix} \quad (\text{A.1})$$

-
- [1] G. Hétet, J. J. Longdell, M. J. Sellars, P. K. Lam, and B. C. Buchler, *Physical Review Letters* **101**, 203601 (2008).
- [2] M. Afzelius, C. Simon, H. de Riedmatten, and N. Gisin, *Physical Review A* **79**, 052329 (2009).
- [3] E. Fraval, M. J. Sellars, and J. J. Longdell, *Physical Review Letters* **92**, 077601 (2004).
- [4] O. Guillot-Noël, P. Goldner, E. Antic-Fidancev, and J. L. Le Gouët, *Physical Review B* **71**, 174409 (2005).
- [5] O. Guillot-Noël, Y. Le Du, F. Beaudoux, E. Antic-Fidancev, M. F. Reid, R. Marino, J. Lejay, A. Ferrier, and P. Goldner, *Journal of Luminescence* **130**, 1557 (2010).
- [6] M. Zhong, M. P. Hedges, R. L. Ahlefeldt, J. G. Bartholomew, S. E. Beavan, S. M. Wittig, J. J. Longdell, and M. J. Sellars, *Nature* **517**, 177 (2015).
- [7] D. P. McLeod and M. F. Reid, *Journal of Alloys and Compounds* **250**, 302 (1997).
- [8] J.-P. R. Wells, G. D. Jones, and R. J. Reeves, *Physical Review B* **60**, 851 (1999).
- [9] P. Goldner and O. Guillot-Noël, *Molecular Physics* **102**, 1185 (2004).
- [10] P. Goldner and O. Guillot-Noël, *Journal of Alloys and Compounds* **451**, 682 (2008).

- [11] M. Popova, E. Chukalina, B. Malkin, and S. Saikin, *Physical Review B* **61**, 7421 (2000).
- [12] K. I. Gerasimov, M. M. Minnegaliev, B. Z. Malkin, E. I. Baibekov, and S. A. Moiseev, *Physical Review B* **94**, 054429 (2016).
- [13] S. P. Horvath, J. V. Rakonjac, Y. H. Chen, J. J. Longdell, P. Goldner, J. P. Wells, and M. F. Reid, *Physical Review Letters* **123**, 057401 (2019).
- [14] M. N. Popova, S. A. Klimin, S. A. Moiseev, K. I. Gerasimov, M. M. Minnegaliev, E. I. Baibekov, G. S. Shakurov, M. Bettinelli, and M. C. Chou, *Physical Review B* **99**, 235151 (2019).
- [15] J. P. R. Wells, G. D. Jones, M. F. Reid, M. N. Popova, and E. P. Chukalina, *Molecular Physics* **102**, 1367 (2004).
- [16] A. Baraldi, R. Capelletti, M. Mazzer, N. Magnani, I. Földvári, and E. Beregi, *Physical Review B* **76**, 165130 (2007).
- [17] M. Mazzer, R. Capelletti, A. Baraldi, E. Buffagni, N. Magnani, and M. Bettinelli, *Journal of Physics: Condensed Matter* **24**, 205501 (2012).
- [18] D. S. Pytalev, E. P. Chukalina, M. N. Popova, G. S. Shakurov, B. Z. Malkin, and S. L. Korableva, *Physical Review B* **86**, 115124 (2012).
- [19] G. S. Shakurov, E. P. Chukalina, M. N. Popova, B. Z. Malkin, and A. M. Tkachuk, *Phys. Chem. Chem. Phys.* **16**, 24727 (2014).
- [20] K. N. Boldyrev, M. N. Popova, B. Z. Malkin, and N. M. Abishev, *Physical Review B* **99**, 041105 (2019).
- [21] S. Mothkuri, M. F. Reid, J.-P. R. Wells, E. Lafitte-Houssat, P. Goldner, and A. Ferrier, *Physical Review B* **103**, 104109 (2021).
- [22] G. K. Liu, J. Huang, R. L. Cone, and B. Jacquier, *Physical Review B* **38**, 11061 (1988).
- [23] J.-P. R. Wells and G. D. Jones, *Physical Review B* **80**, 115105 (2009).
- [24] R. J. Elliott, *Proceedings of the Physical Society. Section B* **70**, 119 (1957).
- [25] R. M. Sternheimer, *Physical Review* **146**, 140 (1966).
- [26] J. Blok and D. A. Shirley, *Physical Review* **143**, 278 (1966).
- [27] A. J. Silversmith, *High Resolution Laser Spectroscopy of Trivalent Europium Centers in Crystals*, Ph.D. thesis, Australian National University (1985).
- [28] B. G. Wybourne, *Spectroscopic Properties of Rare Earths* (Interscience Publishers, 1965).
- [29] M. Weissbluth, *Atoms and Molecules* (Academic Press, 1978).
- [30] G. Liu, in *Spectroscopic Properties of Rare Earths in Optical Materials*, Vol. 83, edited by R. Hull, J. Parisi, R. M. Osgood, H. Warlimont, G. Liu, and B. Jacquier (Springer Berlin Heidelberg, 2005) Chap. 1, pp. 1–94.
- [31] W. T. Carnall, G. L. Goodman, K. Rajnak, and R. S. Rana, *The Journal of Chemical Physics* **90**, 3443 (1989).
- [32] K. Rajnak and B. G. Wybourne, *Physical Review* **132**, 280 (1963).
- [33] B. R. Judd, *Operator Techniques in Atomic Spectroscopy* (Princeton University Press, 1998).
- [34] B. R. Judd, *Physical Review* **141**, 4 (1966).
- [35] H. H. Marvin, *Physical Review* **71**, 102 (1947).
- [36] B. R. Judd, H. M. Crosswhite, and H. Crosswhite, *Physical Review* **169**, 130 (1968).
- [37] C. W. Nielson and G. F. Koster, *Spectroscopic coefficients for the p^n , d^n , and f^n configurations* (M. I. T. Press, 1963).
- [38] C. Görller-Walrand and K. Binnemans, in *Handbook on the Physics and Chemistry of Rare Earths*, Vol. 23 (Elsevier, 1996) Chap. 155, pp. 121–283.
- [39] D. J. Newman and B. Ng, *Reports on Progress in Physics* **52**, 699 (1989).
- [40] R. M. Sternheimer, *Physical Review* **164**, 10 (1967).
- [41] R. M. Sternheimer, *Zeitschrift für Naturforschung - Section A Journal of Physical Sciences* **41**, 24 (1986).
- [42] A. P. Radliński and A. J. Silversmith, *Physical Review B* **34**, 86 (1986).
- [43] Y.-H. Chen, X. Fernandez-Gonzalvo, S. P. Horvath, J. V. Rakonjac, and J. J. Longdell, *Physical Review B* **97**, 024419 (2018).
- [44] R. Macfarlane and R. Shelby, in *Spectroscopy of Solids Containing Rare Earth Ions*, Vol. 21 (Elsevier, 1987) pp. 51–184.
- [45] M. Lovrić, P. Glasenapp, D. Suter, B. Tumino, A. Ferrier, P. Goldner, M. Sabooni, L. Rippe, S. Kröll, M. Lovrić, P. Glasenapp, D. Suter, B. Tumino, A. Ferrier, P. Goldner, M. Sabooni, L. Rippe, and S. Kröll, *Physical Review B* **84**, 104417 (2011), arXiv:1107.2274.
- [46] B. Bleaney, *Physica* **69**, 317 (1973).
- [47] B. R. Judd, C. A. Lovejoy, and D. A. Shirley, *Physical Review* **128**, 1733 (1962).
- [48] M. A. Teplov, *Soviet Journal of Experimental and Theoretical Physics* **26**, 872 (1967).
- [49] M. Lovrić, P. Glasenapp, and D. Suter, *Physical Review B - Condensed Matter and Materials Physics* **85**, 014429 (2012).
- [50] S. Horvath, *High-resolution spectroscopy and novel crystal-field methods for rare-earth based quantum information processing*, Ph.D. thesis, University of Canterbury (2016).
- [51] W. T. Carnall, H. Crosswhite, H. M. Crosswhite, and J. G. Conway, *The Journal of Chemical Physics* **64**, 3582 (1976).
- [52] D. J. Wales and J. P. K. Doye, *The Journal of Physical Chemistry A* **101**, 5111 (1997).
- [53] D. J. Wales, *Science* **285**, 1368 (1999).
- [54] A. J. Silversmith and R. M. MacFarlane, *Physical Review B* **45**, 5811 (1992).
- [55] J. P. R. Wells and R. J. Reeves, *Physical Review B* **64**, 035102 (2001).
- [56] R. M. Shelby and R. M. MacFarlane, *Physical Review Letters* **47**, 1172 (1981).
- [57] A. J. Silversmith and A. P. Radliński, *Journal of Physics C: Solid State Physics* **18**, 4385 (1985).
- [58] A. J. Silversmith and N. B. Manson, *Physical Review B* **34**, 4854 (1986).
- [59] A. J. Silversmith, A. P. Radliński, and N. B. Manson, *Le Journal de Physique Colloques* **46**, C7 (1985).
- [60] A. J. Silversmith, A. P. Radliński, and N. B. Manson, *Physical Review B* **34**, 7554 (1986).
- [61] J. J. Longdell, A. L. Alexander, and M. J. Sellars, *Physical Review B* **74**, 195101 (2006).
- [62] K. Binnemans and C. Görller-Walrand, *Journal of Alloys and Compounds* **250**, 326 (1997).
- [63] N. A. Stump, R. G. Haire, and J. R. Peterson, *Spectroscopy Letters* **32**, 737 (1999).
- [64] N. A. Stump, G. K. Schweitzer, J. K. Gibson, R. G. Haire, and J. R. Peterson, *Applied Spectroscopy* **48**, 937 (1994).
- [65] K. H. Hellwege and H. G. Kahle, *Zeitschrift für Physik* **129**, 62 (1951).

- [66] H. G. Kahle, *Zeitschrift für Physik* **155**, 145 (1959).
- [67] J. Martin, M. Sellars, P. Tuthill, N. Manson, G. Pryde, and T. Dyke, *Journal of Luminescence* **78**, 19 (1998).
- [68] R. Ahlefeldt, *Evaluation of a stoichiometric rare earth crystal for quantum computing*, Ph.D. thesis, Australian National University (2013).
- [69] R. L. Ahlefeldt, D. L. McAuslan, J. J. Longdell, N. B. Manson, and M. J. Sellars, *Physical Review Letters* **111**, 240501 (2013).
- [70] R. L. Ahlefeldt, M. J. Pearce, M. R. Hush, and M. J. Sellars, *Physical Review A* **101**, 012309 (2020).
- [71] N. J. Stone, *Atomic Data and Nuclear Data Tables* **90**, 75 (2005).
- [72] C. Rudowicz and R. Bramley, *The Journal of Chemical Physics* **83**, 5192 (1985).
- [73] C. Rudowicz, M. Chua, and M. Reid, *Physica B: Condensed Matter* **291**, 327 (2000).
- [74] C. Rudowicz, *The Journal of Chemical Physics* **84**, 5045 (1986).
- [75] O. K. Moune and P. Caro, *Journal of the Less Common Metals* **148**, 181 (1989).
- [76] D. Garcia and M. Faucher, in *Handbook on the Physics and Chemistry of Rare Earths*, Vol. 21 (Elsevier, 1995) Chap. 144, pp. 263–304.